JMEPEG (2012) 21:2024–2037
DOI: 10.1007/s11665-011-0117-8

1059-9495/$19.00

# Concept-Level Analysis and Design of Polyurea for Enhanced Blast-Mitigation Performance

*M. Grujicic, B.P. d'Entremont, B. Pandurangan, J. Runt, J. Tarter, and G. Dillon*

*(Submitted November 15, 2011)*

**Polyurea is an elastomeric co-polymer in which the presence of strong hydrogen bonding between chains gives rise to the formation of a nano-composite like microstructure consisting of discrete hard-domains distributed randomly within a compliant/soft matrix. Several experimental investigations reported in the open literature have indicated that the application of polyurea external coatings and/or internal linings can substantially improve ballistic penetration resistance and blast survivability of buildings, vehicles and laboratory/field test-plates. Recently, it was proposed that transition of polyurea between its rubbery state and its glassy state under high deformation-rate loading conditions is the main mechanism responsible for the improved ballistic-impact resistance of polyurea-coated structures. As far as the shock-mitigation performance of polyurea is concerned, additional/alternative mechanisms such as shock-impedance mismatch, shock-wave dispersion, fracture-mode conversion, and strain delocalization have been suggested (without validation). In this study, an attempt is made to identify the phenomena and processes within polyurea which are most likely responsible for the observed superior shock-mitigation performance of this material. Towards that end, computational methods and tools are used to investigate shockwave generation, propagation, dispersion, and transmission/reflection within polyurea and the adjoining material layers as present in the case of a blast-loaded assembly consisting of a head covered with a polyurea-augmented helmet. The results obtained show that for effective shock mitigation, the operation of volumetric energy-dissipating/energy-storing processes is required. Candidate processes of this type are identified and presented.**

**Keywords** impact and ballistic, modeling, polymer

## 1. Introduction

The main objective of this study is to utilize the current state of knowledge of the microstructure-property-performance relations in polyurea to identify phenomena and processes which play (or may play) a dominant role in the well-established superior shock-mitigation performance of this material. Hence, the key aspects of this study are: (a) blast-loading; (b) polyurea; and (c) use of polyurea in blast-mitigation applications. These aspects will be briefly overviewed in the remainder of this section.

### 1.1 Blast-Loading

Blast-waves are high intensity waves which propagate through a fluid medium (e.g., air) and after collision with target structures exert time-dependent loading on to the structures, transferring to them substantial momentum and kinetic energy. Blast-waves are generally produced as a result of intentional or accidental explosions. In the combat theatre, explosions are normally intentional and result from the detonation of various explosives. In the civilian/industrial environment, on the other hand, explosions are often the result of accidents or negligence. Regardless of the circumstances under which explosions occur, there is a general need to develop blast-resistant structures which could protect infrastructure and personnel. Development of such structures is generally costly, time consuming, and involves destructive (one-shot) testing.

To accelerate and reduce the cost of such development, subscale testing and computational engineering analyses are often employed (e.g., Ref 1-5). It is important to note that, for subscale testing and computational analyses applicable to full-scale structures, time-dependent blast-loading must be correctly and accurately accounted for. Failure to do so, as pointed out in Ref 6, may yield erroneous findings. For example, in the analysis of the traumatic brain injury (TBI), of interest in this study, blast-loading is often described by specifying only the peak-overpressure, while the magnitude of the incident specific impulse is down-played. This practice cannot be defended since characterization of blast-loading has to include a complete definition of its time dependence. A more detailed treatment of the time-dependent blast-loading is presented in the next section.

### 1.2 Polyurea

Polyurea is an elastomeric co-polymer in which the presence of strong hydrogen bonding between chains gives rise to the formation of a nano-composite-like microstructure consisting

**M. Grujicic, B.P. d'Entremont,** and **B. Pandurangan**, Department of Mechanical Engineering, Clemson University, 241 Engineering Innovation Building, Clemson, SC 29634-0921; **J. Runt**, Department of Material Science and Engineering, Pennsylvania State University, University Park, PA 16082; and **J. Tarter** and **G. Dillon**, Applied Research Laboratories, Pennsylvania State University, University Park, PA 16082. Contact e-mail: gmica@clemson.edu.

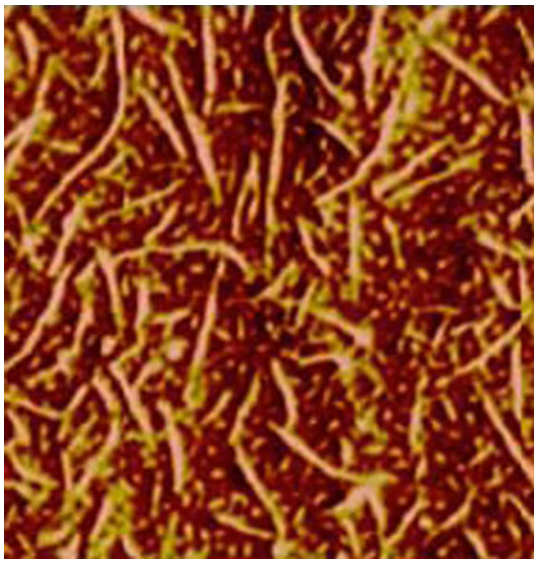

**Fig. 1** A typical tapping-mode AFM phase image of polyurea showing its micro-segregated structure consisting of ribbon-like hard domains and a soft matrix

of discrete hard-domains distributed randomly within a compliant/soft matrix, Fig. 1. The following two features of this material are often cited as being particularly attractive: (a) rapid co-polymerization/gel-reaction times which enable the use of conventional spraying processes for application of polyurea to the structures to be protected; and (b) relatively small modifications in the chemistry and/or synthesis conditions can be employed to alter polyurea microstructure and properties. A detailed analysis of the polyurea molecular-level chemistry and structure was presented in our recent study (e.g., Ref 7, 8) and, hence, will not be repeated here. In short, polyurea chains contain urea linkages (-NH-CO-NH-) which are polar and together with the adjoining di-phenyl methane ($C_6H_5$-$CH_2$-$C_6H_5$) functional groups form the so-called hard (i.e., high-stiffness) segments. In addition to the hard segments, polyurea chains contain soft segments consisting of a series of aliphatic functional groups. Strong hydrogen bonding between urea linkages of the neighboring chains (or the neighboring portions of the same chain) promotes clustering of hard segments into the so-called nanometer-sized hard (i.e., high glass-transition temperature, often crystallized) domains. The remaining hard and the soft segments of the polyurea chains are fairly well-mixed and form the so-called soft (i.e., low glass-transition temperature, amorphous) matrix. It should be noted that strong hydrogen bonding within the hard-domains provides thermo-plastic inter-chain cross-linking. In addition, depending on its chemical make-up and stoichiometry polyurea may contain different extents of covalent-type inter-chain cross-linking.

Due to its complex hierarchical microstructure, polyurea has been found to display quite complex mechanical response under static and dynamic large-strain loading conditions. The main characteristics of the polyurea mechanical response can be defined as (e.g., Ref 9, 10): (a) a high degree of material constitutive non-linearity; (b) highly pronounced temperature (and strain-rate) sensitivity; and (c) extreme pressure dependence arising from the nearly incompressible character of polyurea. To take full advantage of the aforementioned features of polyurea, this material is often used in blast/ballistic-impact protection and abrasion/corrosion prevention applications (e.g., Ref 11-13).

### 1.3 Use of Polyurea in Blast-mitigation Applications

To counter the threats associated with detonation of bombs, ordnance, and improvised explosive devices (IEDs), a new approach has been adopted in recent years that involves the application of polyurea external coatings and/or internal linings to the structures to be protected. The US Air Force first validated this protection strategy by demonstrating an increase in blast survivability in polyurea-sprayed masonry buildings (Ref 14). In addition to preventing structural collapse, polyurea coatings/interior linings were found to contain wall fragments/debris and prevent them from entering the building interior. Since such fragments could be propelled to very high velocities, they have been identified as one of the major causes of injury/fatality of the blast-impacted building occupants. Subsequently, US Navy employed polyurea coatings to enhance ballistic penetration resistance and blast-survivability of its vehicles (e.g., US Marine Corp's High Mobility Multipurpose Wheeled Vehicle, HMMWV) and infrastructure (Ref 15).

When carrying out (experimental or computational) assessments of the blast-mitigation efficacy of various elastomer-coating-based protection strategies, real-life target structures (e.g., building walls and vehicle body panels) are typically replaced with thin/thick plate-like surrogate test-structures. A review of the literature carried out as a part of this study identified a large number of reports dealing with the structural response of the uncoated surrogate test structures to blast-loading. Nurick and Martin (Ref 16), provided recently a fairly comprehensive review of these experimental investigations covering the key aspects associated with the experimental procedures used, the measurements taken and the main findings obtained. In addition, Balden and Nurick (Ref 17) and Lee and Wierzbicki (Ref 18) also overviewed the main analytical/numerical methods (e.g., momentum conservation approach, eigenvalue expansion methods, and wave form approaches, etc.) used to investigate the response of (non-coated) test structures under dynamic loading. As far as the polyurea-coated test structures subjected to blast-loading are concerned, the literature review carried out within this study identified the computational efforts by Chen et al. (Ref 19) and the experimental work by Teklur et al. (Ref 20) and Amirkhizi et al. (Ref 21). While in these studies the superior shock mitigation potential of polyurea was clearly revealed, no attempt was made to identify the responsible mechanism or mechanisms.

Recently, Roland and coworkers (Ref 22) demonstrated that ballistic-penetration resistance of steel test plates can be significantly enhanced using polyurea (or other elastomers)-based coatings. By analyzing a comprehensive set of experimental results pertaining to the temporal and the spatial evolution of the materials present in coated test structures during ballistic impact event and the polyurea time-dependent mechanical response as determined using the dielectric spectroscopy, Roland and coworkers (Ref 22) concluded that phase transition of the polyurea from the rubbery to the glassy state is the most likely mechanism responsible for the beneficial role of polyurea. While initially Roland and coworkers (Ref 22) were uncertain about the role of hydrogen bonding, their later investigations (Ref 23) revealed that hydrogen bonding makes only a minor contribution to the increase in the ballistic

penetration resistance of polyurea-coated test structures. In addition, Roland and coworkers (Ref 22) showed that to maximize the contribution of the rubbery-to-glassy state transition, chain segmental dynamics should be adjusted by placing (through chemical composition modifications) the polyurea glass transition temperature near but slightly below the test temperature. These findings were subsequently confirmed in a comprehensive computational investigation carried out by Grujicic et al. (Ref 10).

Based on the literature overview presented above, it appears that while the mechanism responsible for the increase in the ballistic penetration resistance of polyurea-coated test structure has been identified, the same could not be said for the mechanism(s) responsible for the good shock-mitigation potential of polyurea.

### 1.4 Main Objective

The main objective of this study is to critically assess the phenomenon of planar shock propagation through polyurea to help identify molecular-level processes which are responsible for the observed superior shock-mitigation performance of polyurea.

### 1.5 Organization of the Article

A brief description of air-borne blast-waves and blast-wave-induced loading is presented in section 2. An analysis of planar longitudinal shock wave propagation within polyurea and of the role of material visco-elasticity is presented in section 3. In section 4, an analysis is presented of blast-induced shockwave propagation, reflection, transmission, and interaction within a multi-material core sample encountered in a typical simulation of TBI. A brief discussion of the volumetric viscous energy dissipative processes which can substantially increase the shock mitigation potential of polyurea is presented in section 5. The main conclusions resulting from this study are summarized in section 6.

## 2. Analysis of Blast-Induced Loading

### 2.1 Generation of Air-borne Blast-Waves

Detonation of a free-air/ground-laid explosive charge rapidly converts solid explosive into a highly compressed, rapidly expanding mass of gaseous detonation-products. High-rate expansion of the gaseous detonation products into the surrounding air produces outward-propagating air-borne shock waves (of a spherical shape, in the case of free-air detonation, and a hemispherical shape in the case of ground detonation). Unlike the (smooth/continuous) sound/acoustic waves, shock waves produce discontinuous changes in pressure, density, etc. across the wave front. Figure 2(a) shows a prototypical pressure versus time trace at a fixed point relative to the free-air explosive-detonation location. Examination of Fig. 2(a) reveals that at the time of arrival, $t_a$, of the shock at a given point of interest, pressure experiences an abrupt change (from its initial/ambient value, $P_a$, to a peak value, $P_s$; $P_s - P_a$ is commonly called the "peak over-pressure"). Thereafter, the pressure decreases and at a post-detonation time of $t_a + t_d$ (typically $t_d$ is commonly called the positive phase duration and is on the order of a few tens of microseconds) becomes equal to

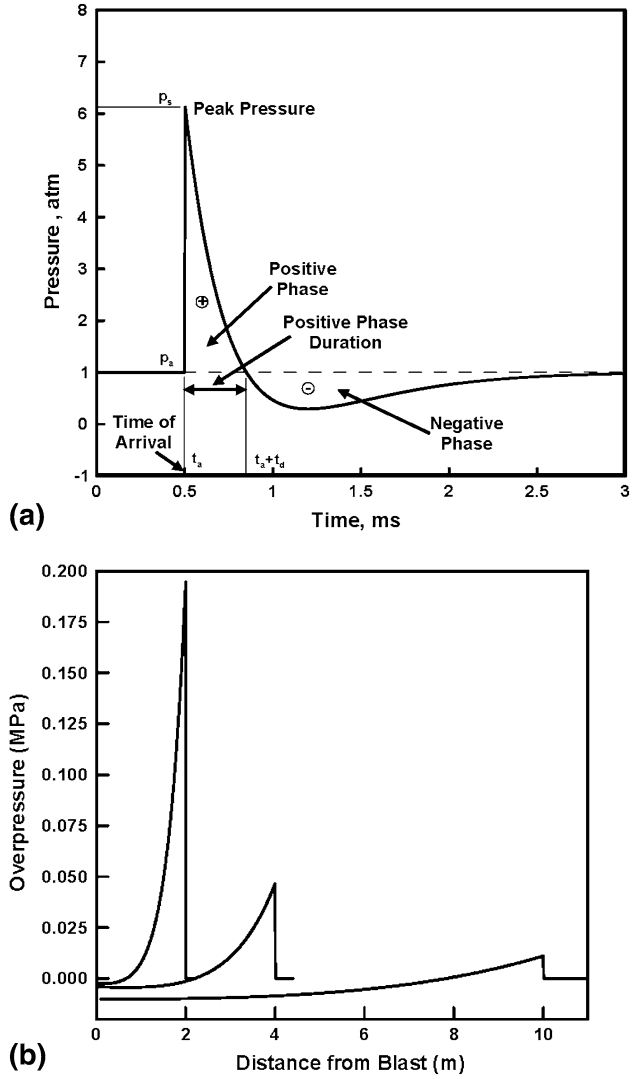


**Fig. 2** (a) A typical free-air pressure versus time relation at a fixed point as defined by the biphasic Friedlander equation; and (b) radial distribution of the blast-induced overpressure associated with 1 kg TNT detonation at post-detonation times of 1.9, 6.4, and 22.7 ms

the ambient pressure, $P_a$. Subsequently, within the so-called suction-phase, the pressure first continues to drop at a progressively lower rate, reaches a minimum and then begins to asymptotically approach the ambient pressure level.

The air-borne blast-wave pressure profile depicted in Fig. 2(a) is usually represented using the biphasic Friedlander functional relation (Ref 24) as:

$$P(t) = (P_s - P_a)e^{-(t-t_a)/\tau}\left[1 - \frac{t-t_a}{t_d}\right] + P_a; \quad t \geq t_a \qquad \text{(Eq 1)}$$
$$P(t) = P_a; \quad \text{otherwise}$$

where τ is a time constant which controls both the rate of pressure decrease from its $P_s$ value and the lowest pressure attained during the suction phase.

When analyzing the interaction of the air-borne blast-wave with a solid structure, one should be cognizant of the fact that there are two components ($P_r$ and $P_i$) of the blast-induced overpressure, $P(t) - P_a$ and that both of these components are defined by the functional relation given in Eq 1. Parameters $t_a$

and $t_d$ are identical for the two components of pressure while the remaining two parameters $P_s$ and $\tau$ generally differ in the two cases. For a general case of a solid surface whose outward normal makes an angle $\theta$ with a vector connecting the surface section to the explosive charge centroid, the total pressure experienced by the target surface is given as

$$P(t) = P_i(t)\left[1 + \cos\theta - 2\cos^2\theta\right] + P_r(t)\cos^2\theta, \quad \cos\theta > 0 \tag{Eq 2a}$$

$$P(t) = P_i(t), \quad \cos\theta \leq 0 \tag{Eq 2b}$$

Examination of Eq 2a reveals that in the case of a target surface which is tangential to the spherically expanding blast-wave ($\cos\theta = 1$), only the reflected component of the pressure ($P_r$) is present. On the other hand, in the case of a target surface that is along one of the radial directions ($\cos\theta = 0$), only the incident pressure component, $P_i$, is present.

Due to the fact that, when a blast-wave strikes the target surface (at a zero obliquity angle) the gas molecules are abruptly brought to rest (conservation of linear momentum demands that) $P_r$ is larger than $P_i$. This overpressure magnification factor is typically around 2.0 in the case of weak blast-waves. Overpressure magnification factors as high as 8.0 and 20.0 have been reported in the case of stronger blast-waves in ideal gas and real gas, respectively (Ref 25). While the plot shown in Fig. 2(a) depicts temporal evolution of the pressure at a fixed stand-off distance (a radial distance from the charge center of mass), it is often useful to show radial distribution of pressure as a function of the post-detonation time. An example of the later plot is depicted in Fig. 2(b) for the case of 1 kg TNT at the post-detonation times (1.9, 6.4, and 22.7 ms) corresponding to blast arrival at the radial locations 2, 4, and 10 m from the charge center of mass. It is seen that as the (spherically shaped) blast-wave expands, it undergoes attenuation and dispersion/spreading.

### 2.2 Parameterization of the Blast-wave Pressure Profile

In the absence of experimental results, the bi-phasic Friedlander blast-wave pressure-profile parameters like $P_s - P_a$, $t_a$, $t_d$, and $\tau$ are often predicted using CONWEP, an empirically based blast simulation code developed by the US Army Corps of Engineers (Ref 26). Within CONWEP (Ref 26), all the incident and the reflected pressure parameters used in Eq 1 are assumed to be functions of a scaled distance (defined as a ratio of (i) the distance between the loaded surface and the explosive charge centroid and (ii) a cube root of the TNT equivalent explosive charge mass). In addition, $t_a$, $t_d$, and $\tau$ are proposal to the cube root of the charge mass.

Until recently, most computational and experimental investigations dealing with the problem of mild-TBI (m-TBI) included blast-wave incident peak overpressures in a 5-20 atm range (e.g., Ref 27-29). It is currently believed that these pressure levels are responsible for more severe TBI cases and that peak overpressures around 1 atm should be investigated in the case of m-TBIs. This level of incident peak overpressure was investigated in this study. However, it should be noted that the incident peak-overpressure does not fully define blast-wave-induced loading since the same incident peak overpressure (controlled by the scaled distance, defined earlier) can be obtained through different combinations of the stand-off distance and the charge mass. In the remainder of this section, the results of a brief investigation are reported which deal with the effect of the stand-off distance (at a constant scaled distance) on various bi-phasic Friedlander blast-wave pressure parameters.

**2.2.1 Peak Overpressure.** Within the CONWEP model, the peak overpressure scales with the scaled distance (defined above). In other words, at a constant peak overpressure, $P_s - P_a$, there is a linear relationship between log(charge mass) and log(stand-off distance) with a slope of one-third. A log(charge mass) versus log(stand-off distance) plot corresponding to the (incident) peak overpressure of 1 atm was computed in this study but not shown for brevity. In accordance with the discussion presented above, incident peak overpressure is invariant to the stand-off distance at a constant level of the scaled distance. An (constant) incident peak overpressure versus stand-off distance plot is also not shown for brevity.

**2.2.2 Arrival Time.** The effect of stand-off distance (at a constant level of the scaled distance) on $t_a$ is depicted in Fig. 3(a).

**2.2.3 Positive Phase Duration.** The effect of stand-off distance (at a constant level of the scaled distance) on $t_d$ is depicted in Fig. 3(b).

**2.2.4 Time Constant.** The effect of stand-off distance (at a constant level of the scaled distance) on $\tau$ is depicted in Fig. 3(c).

**2.2.5 Positive Phase Incident Impulse.** The effect of stand-off distance (at a constant level of the scaled distance) on the (incident) specific impulse (defined as the area underneath the overpressure curve between $t_a$ and $t_a + t_d$) is depicted in Fig. 3(d).

The results depicted in Fig. 3(a) to (d) show that:

(a) It takes the blast-wave more time to reach and to pass through a location which is further away from the detonation site;
(b) The incident specific impulse increases with an increase in the stand-off distance. This finding is significant since frequently in engineering analyses of blast-loading it is only the peak overpressure that is specified and not the associated specific impulse. For complete specification of blast-induced loading, one must define the entire time history of the blast-loading (which would implicitly define both the peak overpressure and the associated specific impulse); and
(c) Another important finding can be obtained by comparing the positive phase duration with the typical time it takes a shock wave generated in the helmet to reach the center of the intra-cranial cavity (ca. 100 μs, Ref 30). Since $t_d$ is greater than the latter time by at least an order of magnitude, Fig. 3(b), the blast-wave loading can be considered as being in the "fully-supported regime" within which the incident pressure does not change significantly with time.

## 3. Polyurea Shockwave Analysis

### 3.1 Problem Formulation

In this section, generation and propagation of shock waves (induced by a 1 atm incident peak overpressure blast-wave) in polyurea is analyzed. The objective of the analysis was to establish the extent of dissipation of the internal and kinetic

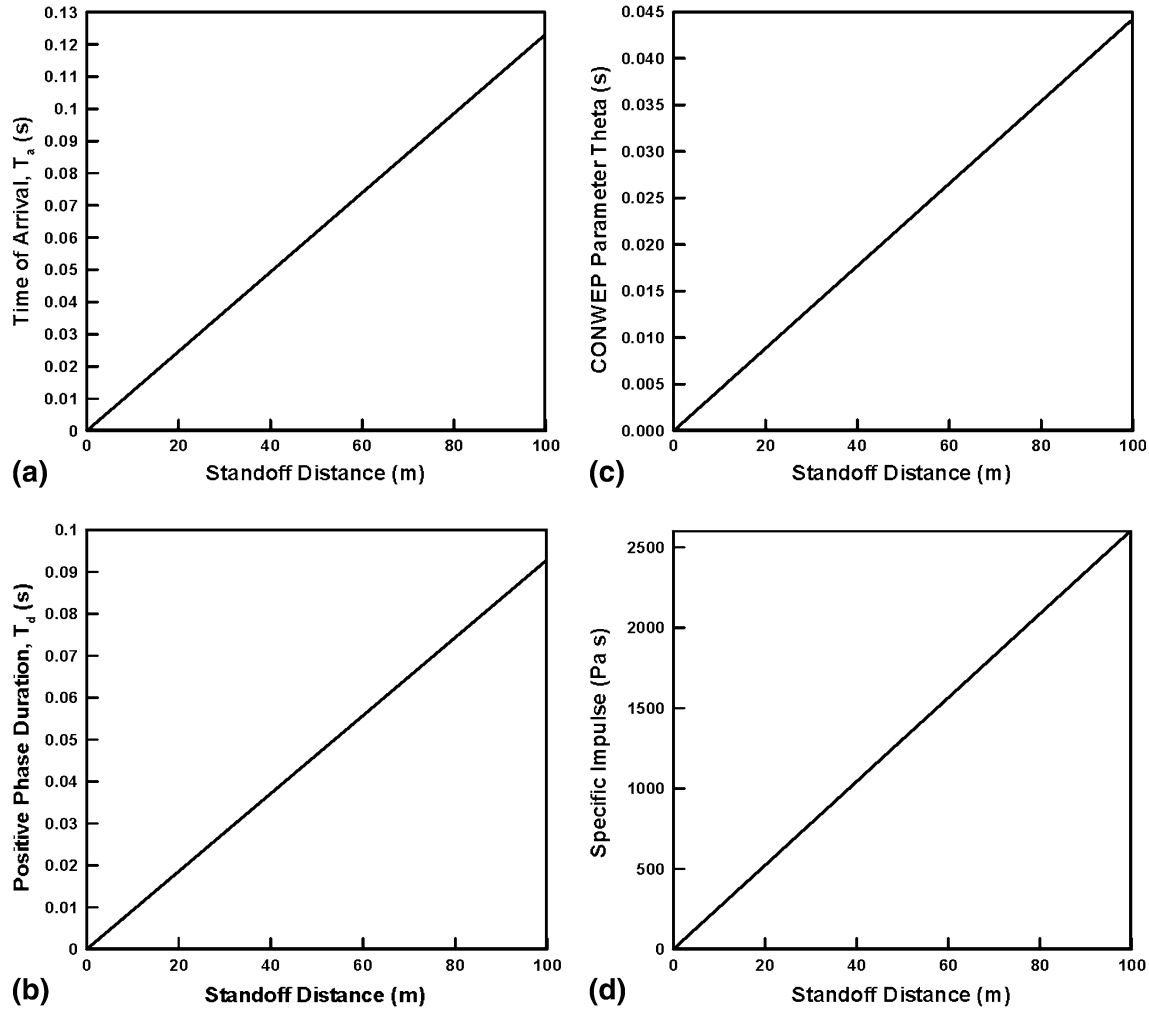


**Fig. 3** The effect of stand-off distance (at a constant value of the scaled distance $Z = 2.70$ m/kg$^{1/3}$, which corresponds to 1 atm peak-overpressure) on: (a) time of arrival; (b) positive phase duration; (c) time constant; and (d) incident specific impulse

energy carried by the shock within polyurea and the associated changes in the shock front profile. In addition, an attempt is made to identify internal phenomena and processes which are responsible for this energy dissipation and to suggest potential ways in which the ability of polyurea to dissipate shock-borne energy can be increased.

### 3.2 Computational Model and Analysis

**3.2.1 Geometrical Model.** Since in most applications polyurea coatings of several millimeters are used, all the calculations carried out in this portion of the study involved a 10 mm thick rectangular parallelepiped polyurea computational domain. The through-the-thickness shock wave is assumed to be of a longitudinal type, i.e., zero-strain boundary conditions are applied in the directions orthogonal to the shock wave propagation direction (no shear strains are allowed). Hence, dimensions of the computational domain in the lateral directions are immaterial.

**3.2.2 Meshed Model.** The geometrical model is meshed in the through-the-thickness direction using 100 first-order reduced integration continuum hexahedron elements of the same thickness.

**3.2.3 Material Model.** To describe the mechanical response of polyurea under blast-loading conditions, the material model reported in Ref 21 was used. Within this model, the hydrostatic response of the material, as defined by the equation of state, is considered to be elastic (non-dissipative) while provisions are made for non-linear geometric effects associated with large deformations/motions of the material. Within the same model, deviatoric response of polyurea is assumed to be time dependent and is treated using a geometrically nonlinear, materially linear, visco-elastic strength model. The time-dependent character of the material's deviatoric purely response is accounted for through four Prony-series terms. These four terms are depicted schematically in Fig. 4, in which a bar-graph is used to show a functional relationship between the visco-elastic relaxation strength and the associated relaxation time. It should be noted that the second bar on the left in Fig. 4, is associated with the chain segmental dynamics and is believed to be responsible for the rubbery-glassy transition in polyurea soft-matrix. Values of all the parameters for the polyurea material model used here can be found in our recent study (Ref 5).

**3.2.4 Initial Conditions.** The computational domain is assumed to be initially stress-free and quiescent (zero velocity).

**3.2.5 Boundary Conditions.** CONWEP loading is applied to one external face (normal to the through-the-thickness direction) of the computational domain and the evolution of the resulting shock wave monitored in small time increments. As mentioned above, zero-velocity boundary conditions are applied to the lateral faces of the computational domain.

**3.2.6 Computational Procedure.** Explicit, transient, non-linear-dynamics finite element analysis is employed while ensuring that the stability criterion is met through the proper and adaptive selection of the time increment. All the calculations carried out in this study were performed using ABAQUS/Explicit (Ref 31).

### 3.3 Results and Discussion

In this section, the results obtained using the polyurea material model described above are first presented. This is followed by a set of results in which changes are made in the polyurea material model to identify phenomena and processes which could be utilized to increase shock mitigation potential of polyurea.

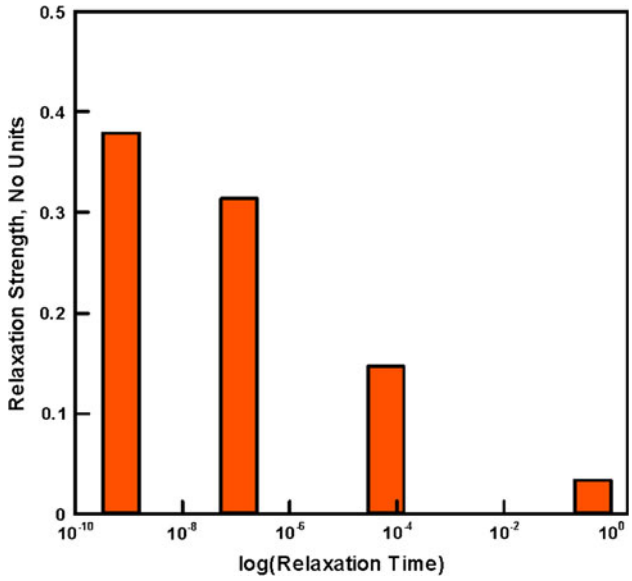


**Fig. 4** Visco-elastic spectrum in the standard formulation of polyurea

**3.3.1 Present Polyurea Material-model Formulation.** Variation of the axial stress through the thickness of the polyurea domain at a post-blast-impact time of 9 μs is depicted in Fig. 5(a). It is seen that the shock wave has nearly reached the free end of the polyurea domain, while a fairly constant axial stress level is found in the as-shocked portion of polyurea (the fully supported shock regime). The axial-stress level is ca. 0.28 MPa, which indicates an amplification factor of approximately 2.8 relative to the incident peak overpressure of 1 atm (=0.1013 MPa). This finding is consistent with the anticipated value (near 2.0) of the amplification factor in the weak-shock regime (discussed in the previous section).

The average shock speed is assessed as 994 m/s. This finding is fully consistent with the experimental values reported in Ref 32.

Examination of Fig. 5(a) shows that the shock-front is quite sharp but of a finite width (ca. 0.7 mm) and continuous due to the operation of the visco-elastic, energy-dissipative processes (as quantified by the four Prony-series terms). It should be noted that no bulk viscosity algorithm was used in the computational analysis so that the shock-front spreading can be entirely attributed to the visco-elastic energy-dissipative processes within polyurea.

The key energy components associated with the shock displayed in Fig. 5(a) are as follows: total strain energy = $3.01 \times 10^{-1}$ J/m$^2$, total kinetic energy = $3.00 \times 10^{-1}$ J/m$^2$, and total visco-elastic dissipative energy = $1.17 \times 10^{-3}$ J/m$^2$. It is seen that the total dissipated energy is only a small fraction (ca. 0.39%) of the total strain energy. This finding is consistent with the fact that under plain-strain uniaxial loading conditions, stress state and, hence, the strain energy is dominated by the volumetric aspects of the material response. Unfortunately, the present polyurea material model does not provide for the volumetric strain energy dissipation or conversion and, consequently, cannot account for the well-established high shock-mitigation potential of polyurea. In the next section, to demonstrate this point more clearly, polyurea cases are considered in which provisions are made for the volumetric strain energy dissipation.

**3.3.2 Modified Polyurea Material-Model Formulation.** The first step towards modifying the present polyurea material model involved closer examination of the four Prony-series visco-elastic terms and identification of the one(s) which

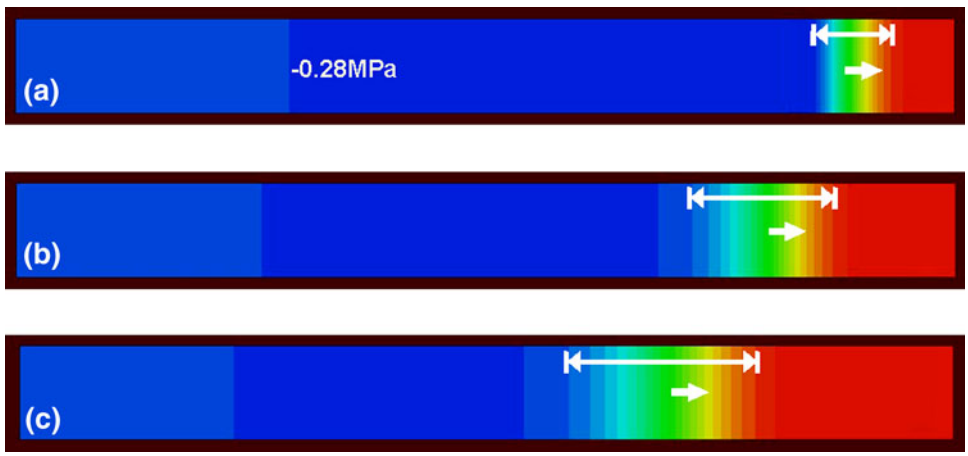


**Fig. 5** Variation of the axial stress through the thickness of the polyurea domain at a post-blast-impact time of 9 μs with different levels of volumetric energy dissipation: (a) no bulk modulus relaxation; (b) bulk modulus relaxation = 20%; and (c) bulk modulus relaxation = 40%

are mainly responsible for the observed shock-energy dissipation. By running a series of computational analyses in which only one Prony-series term was active at a time, it was established that the visco-elastic relaxation process associated with the segmental dynamics (corresponds to the second bar from the left in Fig. 4) provides the dominant contribution to the shock-energy dissipation in polyurea. Results obtained in this portion of the study are summarized in Table 1.

The next step was to identify the optimal relaxation time of the segmental dynamics which maximizes shock-energy dissipation. In this case, the relaxation time associated with the third Prony-series is varied in a range defined by the relaxation times of the fourth and the second Prony-series terms. This portion of the study showed that if the relaxation time is changed from 0.116 to 2.0 μs, the percentage of the energy dissipation increases from 0.38 to 0.74 (at the same magnitude of the associated relaxation strength). In these simulations, relaxation strengths and times for the remaining three Prony-series terms were left unchanged relative to their values displayed in Fig. 4. The effect of the segmental dynamics relaxation time on the percentage energy dissipated is depicted in Fig. 6.

Next, the relaxation strength for the segmental dynamics is increased to a maximum allowable value (i.e., to a value at which the sum of the four relaxation strengths is equal to 1.0) while the relaxation time is set to its optimum value. The resulting percentage visco-elastic energy dissipation increased to ca. 0.93, a value which is still quite small suggesting that volumetric strain-energy dissipative processes must be operative to attain efficient shock mitigation within polyurea.

In the last step of this portion of the study, a non-zero volumetric visco-elastic relaxation strength is assigned to the segmental dynamics term while the remainder of the polyurea material model is retained intact (i.e., the same as given in Fig. 4). Two levels of the volumetric stress relaxation strength (0.2 and 0.4) are considered and they correspond to the maximum bulk modulus relaxation of 20 and 40%, respectively.

Variations of the axial stress through the thickness of the polyurea domain at a post-blast-impact time of 9 μs for the two non-zero bulk modulus relaxation strength levels are depicted in Fig. 5(b) and (c). Comparison of the results displayed in Fig. 5(a) to (c) shows that an increase in the bulk modulus relaxation strength reduces the shock speed and increases the extent of shock-front spreading (the shock width increases). It should be noted that since loading is normal-traction based, the axial-stress level behind the shock is unaffected by the magnitude of the bulk modulus relaxation strength in Fig. 5(a) to (c).

The effect of the bulk modulus relaxation strength on the key energy components associated with the shocks displayed in Fig. 5(a) to (c) is summarized in Table 2. It is seen that the percentage energy dissipated increases from 0.39 to 9.51 as the bulk modulus relaxation strength increases from 0.0 to 0.4. This finding clearly shows the potential of volumetric energy dissipative processes in mitigating shocks. It should be also noted that, as shown in Table 2, the total stored and kinetic energy components also increase as the bulk modulus relaxation strength increases. This finding is a consequence of the fact that CONWEP loading used is surface traction based and does not account for the compliance of the target material. Consequently, the imposed stress level remains fixed while the amount of deformation (and hence the strain energy) increases with the extent of bulk-modulus relaxation. This point was clearly demonstrated in our recent study, in which a more compliant target material (resulting from a higher value of the bulk-modulus relaxation strength) was shown to acquire a smaller level of axial stress and, hence, lower level of the stored and kinetic energies when subjected to a blast-wave modeled explicitly through the use of fluid-structure interaction algorithm.

## 4. Helmeted Head Core Sample Analysis

### 4.1 Problem Formulation

In this section, generation and propagation of shock waves (induced by a 1 atm incident peak overpressure blast-wave) are

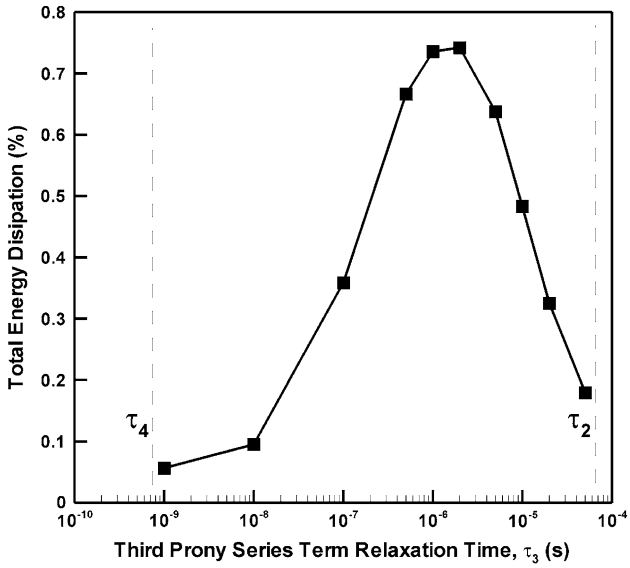


**Fig. 6** Determination of the optimum value of the segmental-dynamics relaxation time for the polyurea formulation in which the remaining three Prony-series terms are left intact

**Table 1 Individual contributions of the four visco-elastic Prony-series terms to the strain energy, kinetic energy and the dissipated energy in polyurea subjected to incident blast-wave loading of 1 atm**

| Prony-series term | Relaxation time, s | Sheer relaxation strength | Total strain energy, J/m$^2$ | Total kinetic energy, J/m$^2$ | Dissipated energy, J/m$^2$ | Fraction of energy dissipated, % |
|---|---|---|---|---|---|---|
| 1 | $4.63 \times 10^{-1}$ | 0.074 | 0.298 | 0.298 | $1.07 \times 10^{-8}$ | $3.89 \times 10^{-1}$ |
| 2 | $6.41 \times 10^{-5}$ | 0.147 | 0.298 | 0.298 | $1.42 \times 10^{-4}$ | $3.61 \times 10^{-6}$ |
| 3 | $1.16 \times 10^{-7}$ | 0.313 | 0.300 | 0.299 | $1.00 \times 10^{-3}$ | $4.76 \times 10^{-2}$ |
| 4 | $7.32 \times 10^{-10}$ | 0.379 | 0.299 | 0.299 | $1.14 \times 10^{-5}$ | $3.34 \times 10^{-1}$ |

**Table 2 The effect of segmental dynamics bulk-modulus visco-elastic relaxation strength on the strain energy, kinetic energy and the dissipated energy in polyurea subjected to incident blast-wave loading of 1 atm**

| Sheer relaxation strength | Total strain energy, J/m$^2$ | Total kinetic energy, J/m$^2$ | Dissipated energy, J/m$^2$ | Fraction of energy dissipated, % |
|---|---|---|---|---|
| 0.000 | 0.301 | 0.300 | 0.300 | 0.389 |
| 0.020 | 0.347 | 0.328 | 0.327 | 5.612 |
| 0.040 | 0.407 | 0.370 | 0.368 | 9.516 |

analyzed within a prototypical core sample encountered in the analyses of blast-wave impact onto a helmet-covered head (often used in the computational investigation of m-TBI). The objective of the analysis was to establish how the potential modifications in polyurea could affect the basic parameter(s) of the intra-cranial shock (peak rise time, peak axial stress, positive phase duration, etc.).

### 4.2 Computational Model and Analysis

**4.2.1 Geometrical Model.** The model used in this study is representative of a helmet-head assembly "core-sample" consisting of a column of single elements running in the direction normal to the helmet outer surface. The column is composed of six segments each associated with a different component of the helmet/head assembly. Starting from helmet and moving inward, the six segments are arranged in the following order: (a) Kevlar/Phenolic-resin composite helmet shell; (b) polyurea suspension pad; (c) skin; (d) skull; (e) the Cerebro-spinal fluid (CSF) and (f) the brain. A schematic of the geometrical model used in this portion of the study along with the associated segment thicknesses (selected to be consistent with the advanced combat helmet design and with the average thicknesses of the skin, the skull, the CSF, and the brain) is depicted in Fig. 7. Also, 0.1 mm initial gaps were assigned at the composite-shell/suspension-pad and the suspension-pad/skull interfaces to account for the fact that these interfaces are neither adhesively bonded nor in complete contact.

**4.2.2 Meshed Model.** Each segment was meshed using first-order reduced integration continuum hexahedron elements with a constant thickness of 50 μm.

**4.2.3 Material Models.** The following material models are used to represent the response of the six segments to dynamic loading:

(a) *Kevlar/Phenolic-Resin Composite Material* Kevlar/Phenolic-resin composite material was represented using a material model within which the hydrostatic part of the stress field is defined using an orthotropic equation of state while the deviatoric response is defined using an orthotropic linear-elastic strength model, as formulated in Ref 33;
(b) *Polyurea Suspension-Pad Material* The polyurea material used for the suspension pads was modeled using the material-model formulation described in section 3.2;
(c) *Skin* The skin (as well as the companion muscle tissue) is treated as a single material and modeled using a Mooney-Rivlin hyperelastic isotropic total-stress formulation;
(d) *Skull* Skull is composed of bone material which is characterized by relatively high levels of hydrostatic and deviatoric rigidity/stiffness. The hydrostatic part of the skull-material model is represented using the Mie-Grunneisen equation of state. Due to the high shear rigidity of skull material and resulting small shear strains, the deviatoric response of this material is defined as linear elastic.
(e) *CSF* The hydrostatic response of the CSF and cerebrum materials is modeled using a Tait-type equation of state, as defined in Ref 28. As far as the deviatoric part of the stress is concerned it is represented using the Neo-Hookean hyperelastic formulation;
(f) *Brain* The same material model (but with a slightly different parameterization) as in the CSF case was used to represent the dynamic response of the brain.

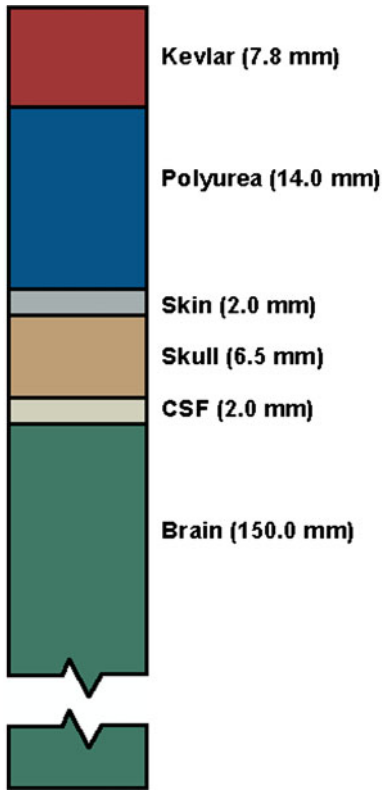


**Fig. 7** Geometrical model of the helmet/head core sample used in the investigation of shock-induced loading and kinematics of the brain. The numbers in brackets indicate layer thicknesses

More details regarding the mathematical formulation and parameterization of the material models presented above can be found in our recent study (Ref 5).

**4.2.4 Initial Conditions.** The computational domain is assumed to be initially stress-free and quiescent (zero velocity).

**4.2.5 Boundary Conditions.** CONWEP loading is applied to one external face (normal to the through-the-thickness direction) of the computational domain and the evolution of the

resulting shock wave monitored in small time increments. As mentioned above, zero-velocity boundary conditions are applied to the lateral faces of the computational domain.

**4.2.6 Contact Conditions.** To model mechanical interactions at the composite-shell/suspension-pad and the suspension-pad/skull interfaces the so-called penalty normal contact algorithm combined with a modified Coulomb friction law is used. Details regarding the treatment of the contacts can be found in our recent study (Ref 8).

**4.2.7 Computational Procedure.** Explicit, transient, non-linear-dynamics finite element analysis is employed while ensuring that the stability criterion is met through the proper and the adaptive selection of the time increment.

### *4.3 Brain Stress/Velocity Results and Discussion*

In this section, the effect of the potential modifications in the polyurea material model on the extent of shock-induced loading (as quantified by the magnitude of the axial stress) and kinematics (as quantified by the magnitude of the axial velocity) of the brain is investigated. The results are first presented for the case of the present polyurea model. This is followed by the ones associated with the modified polyurea model. In the next section, to help rationalize these two sets of results and their differences, a detailed shock propagation, reflection/transmission, and interaction analysis within the core-sample for the two polyurea material model formulations is presented.

**4.3.1 Present Polyurea Material-model Formulation.** Temporal evolution of the negative axial stress in a brain element with the center of mass 25 μs away from the CSF/brain interface is displayed in Fig. 8(a). Examination of this figure reveals that:

(a) The shock arrival time (measured from the moment the blast-wave impacts the outer face of helmet shell) is ca. 50 μs;
(b) The total simulation time (125 μs) is slightly shorter than the time of arrival of the reflected wave from the free end of the brain to the element in question. The arrival of the reflected wave contaminates the loading stress signal being monitored and could not be allowed;
(c) In general, the arrival of the shock wave causes the mean value of the negative axial stress to continuously increase while there are additional oscillatory components of this stress superimposed on to the mean stress; and
(d) At a simulation time of 115 μs, the negative axial stress experiences a peak value of approx. 170 kPa. The associated rise time is 65 μs (115-50 μs).

The temporal evolution of the axial velocity of a brain node which is located at the CSF/brain interface (and is one of the nodes of the element mentioned above) is displayed in Fig. 9(a). Examination of this figure reveals that the axial particle velocity versus time profile closely follows the negative axial stress versus time profile shown in Fig. 8(a). In other words, the shock arrives at ca. 50 μs and after an overall rise time of 65 μs (115-50 μs), the axial velocity reaches a peak value of 40 mm/s.

**4.3.2 Modified Polyurea Material-model Formulation.** Temporal evolution of the negative axial stress in the same brain element as in the case of Fig. 8(a) but for the modified polyurea material model with the bulk modulus relaxation strength of 0.4 is displayed in Fig. 8(b). Examination of this figure reveals that:

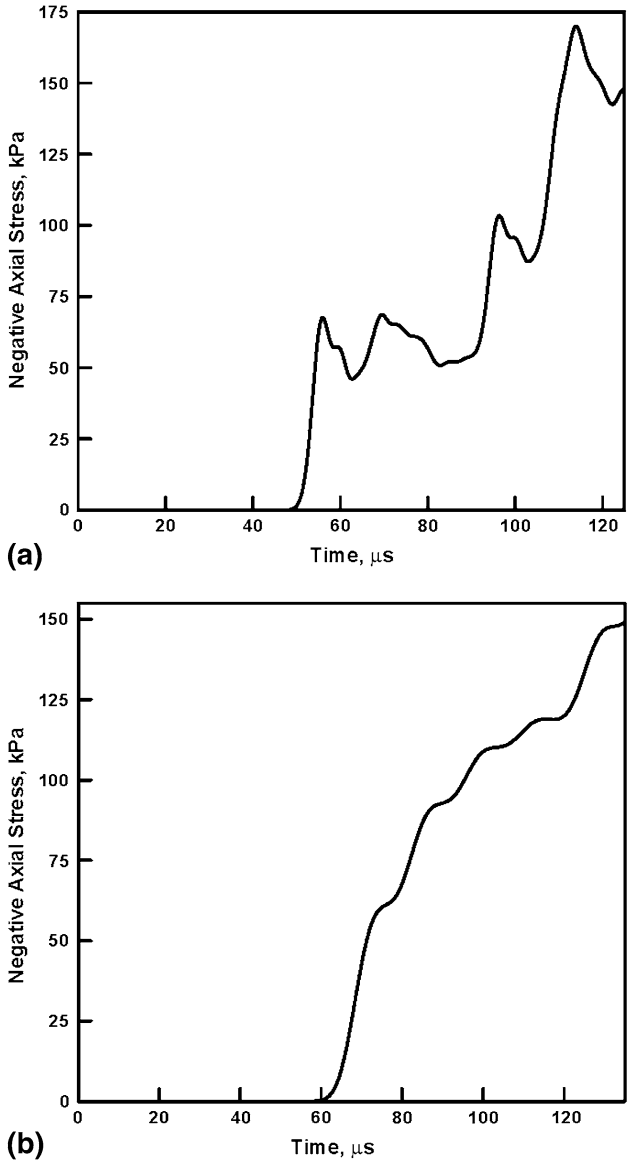


**Fig. 8** Temporal evolution of the negative axial stress in a brain element with the center of mass 25 μm away from the CSF/brain interface for: (a) the present polyurea material model; and (b) the modified polyurea material model (see text for details)

(a) The shock arrival time (measured from the moment the blast-wave impacts the outer face of helmet shell) is ca. 60 μs, which is 10 μs longer than in the present polyurea material model case. This finding is consistent with the fact that a lower value of the polyurea bulk modulus reduces its sound speed/shock velocity;
(b) The total simulation time (135 μs) is again selected in such a way that it is slightly shorter than the time of arrival of the reflected wave from the free end of the brain to the element in question;
(c) As in the case of Fig. 8(a), the arrival of the shock wave causes the mean value of the negative axial stress to continuously increase while there are additional oscillatory

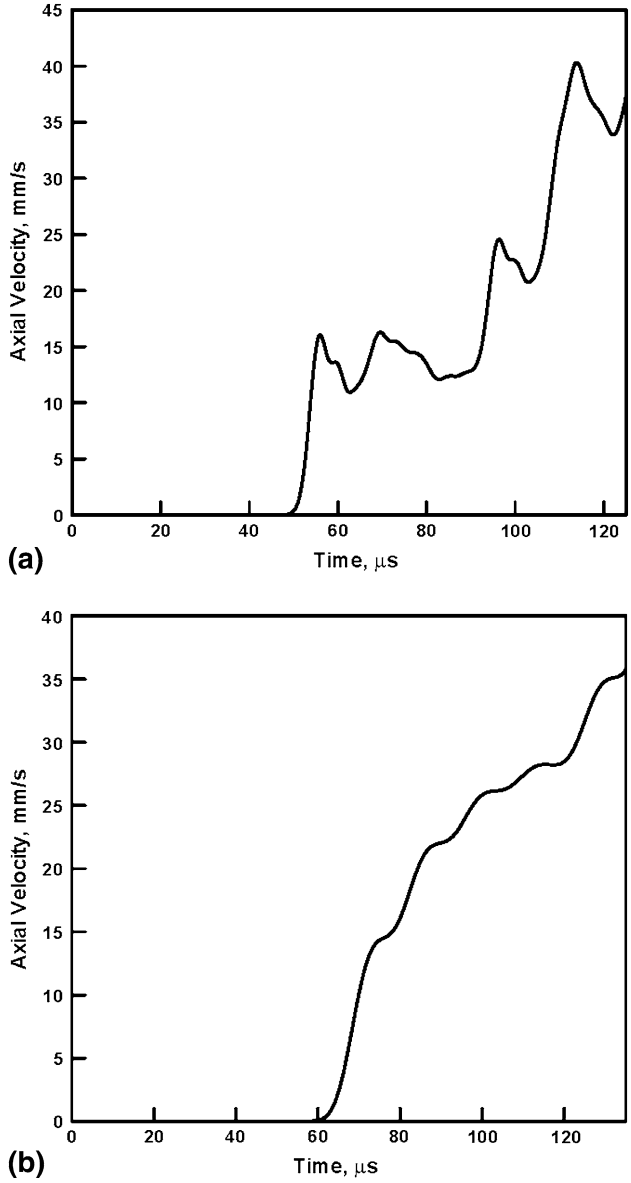


**Fig. 9** Temporal evolution of the axial particle velocity in a brain node at the CSF/brain interface for: (a) the present polyurea material model; and (b) the modified polyurea material model (see text for details)

components of this stress superimposed on to the mean stress. However, the amplitude of these oscillatory waves is substantially smaller; and

(d) After a rise time of 75 μs (135-60 μs), the negative axial stress reaches a maximum value of approx. 148 kPa. This finding shows that the introduction of a bulk-modulus relaxation term into the polyurea material model reduces the maximum value of the negative axial stress within the brain by ca. 13% (from 170 to 148 kPa) while the associated rise time increases by ca. 13% (from 65 to 75 μs). Both of these effects are beneficial from the standpoint of reducing the threat of m-TBI.

The temporal evolution of the axial velocity of at the same brain node as in Fig. 9(a) but for the modified polyurea material model with the bulk modulus relaxation strength of 0.4 is displayed in Fig. 9(b). Examination of this figure reveals that:

(a) The axial particle velocity versus time profile closely follows the negative axial stress versus time profile shown in Fig. 8(b); and

(b) The shock arrives at ca. 60 μs and after an overall rise time of 75 μs, the axial velocity reaches a peak value of 35 mm/s. This is a 13% decrease (from 40 to 35 mm/s) in the axial particle velocity. Since brain motion and its collision with the skull can lead to contusion (a form of m-TBI), this finding further confirms that the introduction of a bulk-modulus relaxation term into the polyurea material model reduces the threat of m-TBI.

### 4.4 Core-Sample Shockwave Propagation Results and Discussion

**4.4.1 Present Polyurea Material-model Formulation.** In Fig. 10(a) to (f), variations of the axial stress along the length of the core sample are presented at six post-impact times: 11, 17, 21, 25, 31, and 39 μs. Examination of Fig. 10(a) to (f) reveals that:

(a) At the shortest time examined, Fig. 10(a), two waves are observed: (i) a release wave traveling to the left within Kevlar/Phenolic helmet shell (a direction opposite to that of the incident blast-wave); and (ii) a (compressive) shock wave propagating to the right within polyurea. These two waves are clearly the result of the interaction of the incident shock within Kevlar/Phenolic helmet shell with the Kevlar/Phenolic resin/polyurea interface and confirm that polyurea has a lower shock impedance than the Kevlar/Phenolic resin;

(b) There are two waves also in Fig. 10(b). However, both are compressive shocks and propagate to the right. The leading shock wave, within polyurea, is the same as the one seen in Fig. 10(a) while the trailing one, within the Kevlar/Phenolic helmet shell is the one generated after reflection of the release wave seen in Fig. 10(a) at the left face of the core sample;

(c) In Fig. 10(c), it is seen that the two shocks arrive at the Kevlar/Phenolic resin/polyurea interface and polyurea/skin interface, respectively, at the same time (as a result of a specific combination of the material model parameters, the layer thicknesses and the loading magnitude);

(d) There are four waves in Fig. 10(d). These waves (two of which are left-propagating release waves while the other two are right-propagating shocks) are the result of the interaction of the two waves shown in Fig. 10(c) with their respective interfaces. It is evident from the position of the leading shock relative to the polyurea/skin interface that shock speeds within skin are quite low;

(e) Figure 10(e) still shows four waves as in the case of Fig. 10(d). However, the left-most wave within Kevlar/Phenolic resin now propagates to the right and has become (after reflection from the core sample left face) a compressive shock. Also, the two previously converging waves within polyurea have crossed and are diverging; and

(f) In Fig. 10(f), there are five waves: (i) a strong left-propagating release wave which is the result of super-position of reflection of a right-propagating shock within the Kevlar/Phenolic resin and a left-propagating transmitted release wave from the polyurea; (ii) a moderate right-propagating

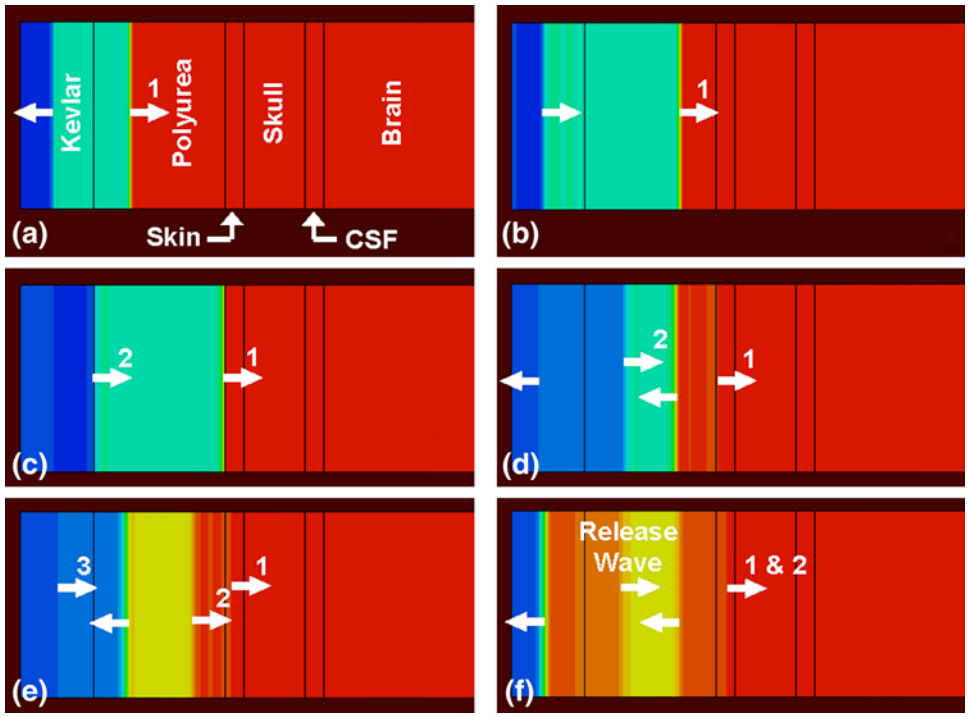


**Fig. 10** Variation of the axial stress along the length of the core sample at six post-impact times: (a) 11 μs, (b) 17 μs, (c) 21 μs, (d) 25 μs, (e) 31 μs, and (f) 39 μs with the present polyurea material model (see text for details)

release wave within polyurea which is the result of super-position of reflection of a left-propagating release wave within the polyurea and a weak right-propagating transmitted shock wave from the Kevlar/Phenolic resin; (iii) a left-propagating reflected release wave which originated at the polyurea/skin interface; (iv) and (v) are two right-propagating nearly superimposed shocks within the skin.

By carefully tracking the transmission of the shock (and ultimately release) waves from the skin into the CSF and, in turn, into the brain, one can establish a correlation between the results displayed in Fig. 8(a) and 10(a) to (f).

**4.4.2 Modified Polyurea Material-model Formulation.** In Fig. 11(a) to (f), variations of the axial stress along the length of the core sample are presented at the same six post-impact times, but for the case of the modified polyurea material formulation. Examination of Fig. 11(a) to (f) reveals that:

(a) At the shortest time examined, Fig. 11(a), two waves are observed as in Fig. 10(a). The origin of the two waves has not changed, but a reduction in the shock speed and an increase in the shock width in polyurea are evident;
(b) Again there are two waves in Fig. 11(b) and they are of the same type as in Fig. 10(b);
(c) Further evidence for the lower shock speed and for shock-front spreading within polyurea can be obtained by comparing Fig. 10(c) and 11(c). Specifically, the distance travelled by the leading shock wave in Fig. 11(c) is roughly half of that in Fig. 10(c);
(d) As a consequence of the fact that the leading shock wave did not reach the polyurea/skin interface, there are only three waves in Fig. 11(d) and not four as in Fig. 10(d);
(e) In Fig. 11(e), there are three right-propagating compression shocks. Two of which are located within polyurea and the remaining one within Kevlar/Phenolic resin; and
(f) In Fig. 11(f), there are three right-propagating shocks within polyurea and one left-propagating release wave within the Kevlar/Phenolic resin. Due to the fact that the three shocks are spread-out and closely spaced they form a large-width finite amplitude compression wave. As far as the release wave is concerned, it is weaker than in Fig. 10(f) since it is only the result of the shock wave reflection at the Kevlar/Phenolic resin/polyurea interface.

By carefully tracking the transmission of the shock (and ultimately release) waves from the skin into the CSF and, in turn, into the brain, one can establish a correlation between the results displayed in Fig. 8(b) and 11(a) to (f).

## 5. Final Discussion

The results presented in the previous section clearly demonstrated that to obtain a significant extent of strain energy dissipation associated with a plane longitudinal shock within polyurea (and the associated reductions in the intra-cranial stresses and velocities), the presence of volumetric viscous damping processes is required. It should be noted that, while not analyzed in this study, similar benefits could be expected from volumetric energy storing processes. Examination of the public domain literature regarding the mechanical behavior and the microstructural modifications/reorganizations accompanying dynamic loading in polyurea identified several potential candidates for these processes. Among these processes, the most prominent ones are: (a) strain-induced crystallization of

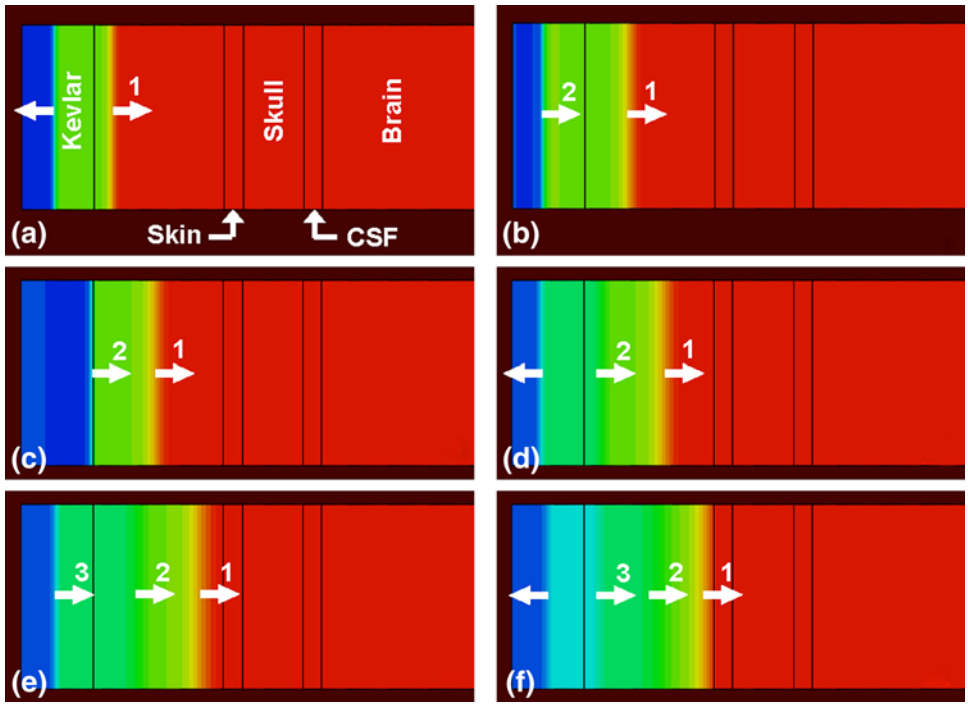


**Fig. 11** Variation of the axial stress along the length of the core sample at six post-impact times: (a) 11 μs, (b) 17 μs, (c) 21 μs, (d) 25 μs, (e) 31 μs, and (f) 39 μs with the modified polyurea material model (see text for details)

the soft matrix; (b) strain-induced crystallization of the hard domains; and (c) realignment of the hard-domains with the principal direction of deformation (which is accompanied by realignment and closer packing of the surrounding soft matrix chain segments). In the remainder of this section, a brief description is provided of these three processes.

### 5.1 Strain-Induced Soft-Matrix Crystallization

In general, polymers may be associated with different levels of crystallinity depending on their molecular structure, processing conditions, glass transition temperature ($T_g$), and melting temperature ($T_m$). It should be recognized that crystallization (promoted by non-covalent chain/chain interactions) in polymers is generally of a short-range character and differs from the long-range crystalline structures found in materials based on small molecules and inorganic materials. Polymer quenching below $T_g$ suppresses crystallization reaction kinetically (i.e., while there is a relatively large thermodynamic driving force for crystallization, chain segments are immobile and are incapable of overcoming the crystallization activation energy barrier). Exposure of a polymer to temperatures between $T_g$ and $T_m$ may lead to crystallization. Due to the competition between chain mobility (increases with temperature) and crystallization thermodynamic driving force (decreases with temperature), there is typically a characteristic temperature in the $T_g - T_m$ range at which the rate of crystallization is maximum.

In addition to overcoming the crystallization activation-energy barrier through an increase in temperature, mechanical energy can have a similar effect during deformation. This phenomenon is commonly referred to as ''strain-induced crystallization'' (Ref 34-36). It is generally believed that the mechanical effects facilitate the crystallization process by decreasing the configurational entropy of the non-crystalline phase. That is, as the molecules of the non-crystalline phase are aligned with the deformation principal direction(s), the associated configurational entropy is decreased and the free energy increased. This, in turn, lowers the crystallization activation-energy barrier. Numerous examples of strain-induced crystallization in polymers have been reported in the open literature (e.g., Ref 37-40). As far as polyurea is concerned, there are few reports of the same (e.g., Ref 35). In Ref 35, it was reported that in polyurea formulation based on poly-tetra-methylene-oxide as soft-segments wide-angle x-ray scattering data provide a clear proof for strain-induced soft segment crystallization. Similar finding has been reported in Ref 41 but for the case of polyurea formulation with poly-dimethyl-siloxane as soft segments.

In addition to the thermal and mechanical effects discussed above, which affect the crystallization process, molecular structure of the polymer itself, in general (and of the polyurea soft-matrix, in particular), also influences the strain-induced crystallization process. Specifically, two aspects of the molecular structure are found to affect the crystallization propensity of polyurea. These two aspects of the polyurea soft-matrix molecular structure include: (a) molecular weight/length of the soft matrix segments; and (b) the extent of inter-chain (covalent-type) cross-linking. In general, longer and more flexible soft-matrix segments tend to be more mobile and, hence, are more prone to forming crystalline structures. On the other hand, covalent-type cross-linking hampers segmental mobility and interferes with the crystallization process. Thus, to increase the extent of strain-induced crystallization in polyurea soft-matrix, polyurea formulations based on high molecular weight $R'$ functional groups with a low extent of covalent-type cross-linking are preferred. This suggests that polyurea based on Isonate 143L and Versalink P1000 which is associated with a significant extent of cross-linking is less favorable than the

one based on polymeric-MDI and Versalink P1000 (with significantly lower extent of cross-linking). Also, the polyurea formulations based on smaller-molecular weight (and, hence, stiffer) $R'$ functional groups (Versalink P650 and P250) appear to be less favorable from the standpoint of attaining significant extent of strain-induced polyurea soft-matrix crystallization.

### 5.2 Strain-Induced Hard-Domain Crystallization

As explained earlier, hard-domains are formed as a result of a micro-phase segregation process from fully mixed polyurea as a result of strong hydrogen bonding between urea linkages of the neighboring chains. Hard domains are characterized by a relatively high (250 °C) glass-transition temperature and are often found to contain some fraction of the crystalline phase in the as-cast condition. Clearly, due to a large difference between $T_g$ and the room temperature, no continuous thermally activated crystallization of hard-domains at room-temperature is expected. However, strain-induced crystallization of hard-domains is still possible considering the fact that hard-domains are often found to re-orient themselves in the principal direction of deformation (morphological texture). This re-orientation is expected to be accompanied by additional internal restructuring/crystallization of the hard-domains. Direct evidence of strain-induced crystallization of the hard-domains in polyurea has not been reported (to the best knowledge of the present authors) in the open literature, since it has not been the main subject of any investigation. However, careful examination of some of the wide angle x-ray diffraction (WAXD) and small angle x-ray scattering (SAXS) results reported in Ref 41 suggest that an increase in the extent of crystallization may occur during shock and ballistic-impact loading. In that case, the observed superior penetration resistance and shock mitigation capability of polyurea may be partly attributed to this process. In any case, more detailed experimental microstructure characterization of the polyurea samples which have been first subjected to different levels of ballistic/shock-loading is required.

### 5.3 Strain-Induced Hard-domain Realignment

While, in as-cast polyurea, the hard-domains are randomly oriented, during deformation they tend to align their major axis with the principal direction of deformation (Ref 40). Under such conditions, one would expect that chain segments in the soft-matrix adjacent to the hard-domains would also tend to align themselves with the principal direction of deformation. This process would result in a local increase in the extent of soft-matrix crystallization. In general, one would expect that more flexible soft-matrix chains would tend to undergo a larger extent of local alignment and crystallization. Therefore, to maximize these aspects of soft-matrix crystallization, one would again choose polyurea formulations with large molecular weight $R'$ functional groups (and a lesser extent of cross-linking).

### 5.4 Materials-By-Design

In this study, transient non-linear dynamics analyses are carried out of a blast-loaded polyurea slug and a blast-loaded helmet/head core sample to identify the aspects of polyurea material model which strongly affect the shock-mitigation capacity of this material. Next, intrinsic phenomena and processes associated with these aspects of polyurea mechanical response are identified. Finally, potential modifications in the polyurea chemistry have been identified which would give rise to an increase in the shock-mitigation potential of polyurea. This is an example of the so-called materials-by-design approach within which component level performance results are used to guide the development of new high-performance materials.

## 6. Conclusions

Based on the results obtained in this study, the following main summary remarks and conclusions can be drawn:

1. The parameters characterizing blast-wave temporal evolution and spatial distribution, as encountered in the context of TBI, is analyzed, showing that the impacted structures are under the supported-shock loading regime.
2. Propagation of a planar longitudinal wave with polyurea and its interaction with the viscous energy dissipative processes within polyurea is analyzed to identify specific processes which control the shock-mitigation potential of polyurea.
3. The effect of various viscous energy dissipation processes within polyurea (when used as lining of a head-protection gear/helmet) on the temporal evolution of intra-cranial stresses and velocities is studied.
4. Specific recommendations are made concerning the chemical formulation of polyurea that would maximize the shock-mitigation performance of this material.


## Acknowledgments

The material presented in this article is based on study supported by the Office of Naval Research (ONR) research contract entitled ‘‘Elastomeric Polymer-By-Design to Protect the Warfighter Against Traumatic Brain Injury by Diverting the Blast Induced Shock Waves from the Head’’, Contract Number 4036-CU-ONR-1125 as funded through the Pennsylvania State University. The authors are indebted to professors G. Settles and M. Hargather for stimulating discussions and friendship.


## References


1. M. Grujicic, H. Marvi, G. Arakere, W.C. Bell, and I. Haque, The Effect of Up-armoring the High-Mobility Multi-purpose Wheeled Vehicle (HMMWV) on the Off-road Vehicle Performance’’, *Multidiscip. Model. Mater. Struct.*, 2010, **6**(2), p 229–256
2. M. Grujicic, W.C. Bell, G. Arakere, and I. Haque, Finite Element Analysis of the Effect of Up-armoring on the Off-road Braking and Sharp-turn Performance of a High-Mobility Multi-purpose Wheeled Vehicle (HMMWV), *J. Automob. Eng.*, 2009, **223**(D11), p 1419–1434
3. M. Grujicic, G. Arakere, H.K. Nallagatla, W.C. Bell, and I. Haque, Computational Investigation of Blast Survivability and Off-road Performance of an Up-armored High-Mobility Multi-purpose Wheeled Vehicle (HMMWV), *J. Automob. Eng.*, 2009, **223**, p 301–325
4. M. Grujicic, G. Arakere, B. Pandurangan, W.C. Bell, T. He, and X. Xie, Material-modeling and Structural-mechanics Aspects of the Traumatic Brain Injury Problem, *Multidiscip. Model. Mater. Struct.*, 2010, **6**(3), p 335–363
5. M. Grujicic, W.C. Bell, B. Pandurangan, and P.S. Glomski, Fluid/Structure Interaction Computational Investigation of the Blast-Wave Mitigation Efficacy of the Advanced Combat Helmet, *J. Mater. Eng. Perform.*, 2011, **20**(6), p 877–893

6. V. F. Nesterenko, Shock (Blast) Mitigation by "Soft" Condensed Matter, *MRS Symposium Proceedings*, **751**, 2003, MM 4.3.1–MM 4.3.12
7. M. Grujicic, T. He, and B. Pandurangan, Development and Parameterization of an Equilibrium Material Model for Segmented Polyurea, *Multidiscip. Model. Mater. Struct.*, 2011, **7**(2), p 96–114
8. M. Grujicic, T. He, and B. Pandurangan, Experimental Characterization and Material-model Development for Microphase-segregated Polyurea: An Overview, *J. Mater. Eng. Perform.* 2010. doi:10.1007/s11665-011-9875-6
9. A.J. Ryan, Spinodal Decomposition during Bulk Copolymerization: Reaction Injection Molding, *Polymer*, 1989, **31**, p 707
10. M. Grujicic, B. Pandurangan, T. He, B.A. Cheeseman, C.-F. Yen, and C.L. Randow, Computational Investigation of Impact Energy Absorption Capability of Polyurea Coatings via Deformation-Induced Glass Transition, *Mater. Sci. Eng. A*, 2010, **527**(29–30), p 7741–7751
11. Y.A. Bahei-El-Din, G.J. Dvorak, and O.J. Fredricksen, A Blast-tolerant Sandwich Plate Design with a Polyurea Interlayer, *Int. J. Solids Struct.*, 2006, **43**, p 7644–7658
12. S. M. Walsh, R. R. Scott and D. M. Spagnuolo, *The Development of a Hybrid Thermoplastic Ballistic Material with Application to Helmets*, ARL-TR-3700, Army Research Laboratory, December 2005
13. S.A. Tekalur, A. Shukla, and K. Shivakumar, Blast Resistance of Polyurea-Based Layered Composite Materials, *Compos. Struct.*, 2008, **84**(3), p 271–281
14. J.R. Porter, R.J. Dinan, M.I. Hammons, and K.J. Knox, Polymer Coatings Increase Blast Resistance of Existing and Temporary Structures, *AMPTIAC Q.*, 2002, **6**(4), p 47–52
15. W. Matthews, Polymer Protection, *Defense News*, 2004, p 32–35
16. G.N. Nurick and J.B. Martin, Deformation of Thin Plates Subjected to Impulsive Loading—A Review, Part II: Experimental Studies, *Int. J. Impact Eng.*, 1989, **8**(2), p 171–186
17. V.H. Balden and G.N. Nurick, Numerical Simulation of the Post-failure Motion of Steel Plates Subjected to Blast Loading, *Int. J. Impact Eng.*, 2005, **32**, p 14–34
18. Y. Lee and T. Wierzbicki, Fracture Prediction of Thin Plates under Localized Impulsive Loading. Part II: Discing and Petalling, *Int. J. Impact Eng.*, 2005, **31**, p 1277–1308
19. C. Chen, D.G. Linzell, E. Alpman, and L.N. Long, Effectiveness of Advanced Coating Systems for Mitigating Blast effects on Steel Components, *Tenth International Conference on Structures Under Shock or Impact*, 14–16 May, 2008, Algarve, Portugal
20. S.A. Tekalur, A. Shukla, and K. Shivakumar, Blast Resistance of Polyurea based Layered Composite Materials, *Compos. Struct.*, 2008, **84**, p 271–281
21. A.V. Amirkhizi, J. Isaacs, J. McGee, and S. Nemat-Nasser, An Experimentally-based Constitutive Model for Polyurea, Including Pressure and Temperature Effects, *Philos. Mag.*, 2006, **86**(3), p 5847–5866
22. R.B. Bogoslovov, C.M. Roland, and R.M. Gamache, Impact-induced Glass-Transition in Elastomer Coatings, *Appl. Phys. Lett.*, 2007, **90**, p 221910
23. C.M. Roland and R. Cassini, Effect of Hydrostatic Pressure on the Viscoelastic Response of Polyurea, *Polymer*, 2007, **48**, p 5747–5752
24. F.G. Friedlander, *The Wave Equation on a Curved Space-Time*, Cambridge Monographs on Mathematical Physics, 2, 1976, Cambridge University Press, New York
25. P.W. Cooper, *Explosives Engineering*, Wiley-VCH, New York, 1996
26. D. Hyde, *User's Guide for Microcomputer Programs, CONWEP and FUNPRO—Applications of TM 5-855-1, U.S*, Army Engineer Waterways Experimental Station, Vicksburg, 1988
27. M.K. Nyein, A.M. Jason, L. Yu, C.M. Pita, J.D. Joannopoulos, D.F. Moore, and R.A. Radovitzky, In Silico Investigation of Intracranial Blast Mitigation with Relevance to Military Traumatic Brain Injury, *Proc. Natl. Acad. Sci. USA*, 2010, **48**(107), p 20703–20708
28. D.F. Moore, R. Radovitzky, L. Shupenko, A. Klinoff, M.S. Jaffee, and J.M. Rosen, Blast Physics and Central Nervous System Injury, *Futur. Neurol.*, 2008, **64**, p S30
29. M.R. Amini, J. Simon, and S. Namet-Nasser, Numerical Modeling of Effect of Polyurea on Response of Steel Plates to Impulsive Loads in Direct Pressure Pulse Experiments, *Mech. Mater.*, 2010, **42**, p 615–627
30. P.A. Taylor and C.C. Ford, Simulation of Blast-induced Early-time Intracranial Wave Physics Leading to Traumatic Brain Injury, *J. Biomech. Eng.*, 2009, **131**, p 061007-1–061007-11
31. ABAQUS Version 6.10 EF1, User Documentation, Dassault Systems, 2010
32. W. Mock, S. Bartyczak, G. Lee, J. Fredderly, and K. Jordan, Dynamic Properties of Polyurea-1000, *Shock Compression of Condensed Matter 2009: Proceedings of the American Physical Society Topical Group on Shock Compression of Condensed Matter*, Vo1. 195, 2009, p 1241–1244
33. ANSYS/Autodyn-2D and 3D, Version 6.1, User Documentation, ANSYS Inc., 2007
34. S. Curgul, I. Yilgor, E. Yilgor, B. Erman, and M. Cakmak, Effect of Chemical Composition on Large Deformation Mechanooptical Properties of High Strength Poly(urethane urea)s, *Macromolecules*, 2004, **37**, p 8676–8685
35. F. Yeh, B.S. Hsiao, B.B. Sauer, S. Michel, and H.W. Siesler, In-Situ Studies of Structure Development during Deformation of a Segmented Poly(urethane urea) Elastomer, *Macromolecules*, 2003, **36**, p 1940–1954
36. R.S. Waletzko, L.T. James Korley, B.D. Pate, E.L. Thomas, and P.T. Hammond, Role of Increased Crystallinity in Deformation-induced Structure of Segmented Thermoplastic Polyurethane Elastomers with PEO and PEO-PPO-PEO Soft Segments and HDI, Hard Segments, *Macromolecules*, 2009, **42**, p 2041–2053
37. M. Tosaka, Strain-Induced Crystallization of Crosslinked Natural Rubber as Revealed by X-ray Diffraction using Synchrotron Radiation, *Polym. J.*, 2007, **39**, p 1207–1220
38. A.N. Gent, S. Kawahara, and J. Zhao, Crystallization and Strength of Natural Rubber and Synthetic cis-1,4-Polyisoprene, *Rubber Chem. Technol.*, 1998, **71**, p 668–678
39. C.I. Martins and M. Cakmak, Control of the Strain-induced Crystallization of Polyethylene Terephthalate by Temporally Varying Deformation Rates: A Mechano-optical Study, *Polymer*, 2007, **48**(7), p 2109–2123
40. M.M. Caruso, D.A. Davis, Q. Shen, S.A. Odom, N.R. Sottos, S.R. White, and J.S. Moore, Mechanically-Induced Chemical Changes in Polymeric Materials, *Chem. Rev.*, 2009, **109**, p 5755–5798
41. J.P. Sheth, A. Aneja, G.L. Wilkes, E. Yilgor, G.E. Atilla, I. Yilgor, and L. Beyer, Influence of System Variables on the Morphology and Dynamic Mechanical Behavior of Polydimethylsiloxanebased Segmented Polyureathane and Polyurea Copolymers: A Comparative Perspective, *Polymer*, 2004, **45**, p 6919–6932